Nickel selenide supported on nickel foam as an efficient and durable non-precious electrocatalyst for the alkaline water electrolysis

Arumugam Sivanantham, Sangaraju Shanmugam *

Department of Energy Systems Engineering, Daegu Gyeongbuk Institute of Science & Technology (DGIST), Daegu 42988, Republic of Korea

A B S T R A C T

Herein, we describe an *in-situ* hybridization of Nickel Selenide (Ni_3Se_2) with a Nickel Foam (NF) current collector as an efficient, ultra-durable electrode for the continuous alkaline water electrolysis. Earth abundant, cost effective, non-precious self-made Ni_3Se_2/NF electrode delivers an oxygen evolution reaction (OER) overpotential value of 315 mV at a current density of 100 mA cm^{-2} (versus a reversible hydrogen electrode) in aqueous electrolyte of 1 M KOH. On a static current density of 100 mA cm^{-2}, Ni_3Se_2/NF electrode shows a good OER stability over 285 h with very small potential loss of 5.5% in alkaline electrolyte. Accordingly, the alkaline water electrolyzer constructed with Ni_3Se_2/NF (anode) and $NiCo_2S_4$/NF (cathode), it requires 1.58 V to deliver 10 mA cm^{-2} current density, with 500 h continuous operation in 1 M KOH. In addition, we demonstrate that the light-driven water splitting using solar panel, it can be a promising approach to facilitate true independence from electricity in H_2 fuel economy. Overall, this methodology is one of the appropriate energy efficient ways to reduce the cost of water splitting devices, as it may simplify the diverse process and equipment.

© 2016 Elsevier B.V. All rights reserved.

1. Introduction

Continuous hydrogen fuel generation from water with low overpotential, ultra-durable non-precious electrocatalyst is a key concern to lower the cost of water-splitting devices, and increase the large scale hydrogen production plants to overcome the fuel demand in the upcoming era [1–3]. Solar light assisted water splitting is a current strategy in hydrogen production due to the use of cost free electricity delivered from the nature [4] and [5]. Accordingly, nature offers the unlimited resource for hydrogen (water) and voltage (solar light) for cost effective generation of hydrogen fuel. The electrochemical reaction occurs on the electrode-electrolyte interface is a potential approach to produce hydrogen, in particularly the oxygen evolution reaction (OER) is a sluggish kinetic half-reaction and challenging, because of several proton-coupled electron transfer stages, it needs larger overpotential [6,7]. Interestingly, in water splitting process ($2H_2O + energy \leftrightarrow 2H_2 + O_2$), one mole of oxygen evolution in anode gives two moles of hydrogen evolution in cathode, then, the OER is most important and unavoidable reaction in the water electrolysis [8]. Suitable OER electrocatalysts are needed to reduce the overpotential by lower-

ing the reaction barrier. Moreover, it should be earth abundant and inexpensive materials for large scale applications. These requirements prompted the researchers to find the most active, stable, earth abundant, low-cost electrocatalysts to completely eliminate the use of precious (RuO_2, IrO_2, Pt/C) electrocatalysts in water splitting technology.

Recently, transition metals and their derivatives (oxides, hydroxides or metal-alloys) have been extensively established as promising OER electrocatalysts [9–13]. In some specific cases, few electrocatalysts exhibit the comparable OER performance with the state-of-the-art electrocatalysts, such as RuO_2 and IrO_2 [14,15]. For example, cobalt and manganese based (Co_3O_4 and Mn_2O_3) electrocatalysts are inexpensive and suitable for OER [16,17]. Nevertheless, still significant improvement is required to reduce the OER overpotential of electrocatalysts for the potential use in the water splitting devices.

Aforementioned drawbacks emphasis that the feasible factors which can improve the oxygen evolution reaction and durability in alkaline conditions are: (i) Porous electrocatalysts able to utilize their maximum active sites in the electrochemical reaction through an efficient electrode-electrolyte interface formation. In particular, during the gas evolution reactions, the formed gas bubbles can easily escape from the each part of electrocatalysts in an efficient way without damaging the electrode surface, which is one of the most important issues in the vigorous and continuous gas

---

evolution environments [18–20]. (ii) Structural stability of electrocatalysts is support, also acts as good current collector for the efficient electron transport. In particular, 3D porous electrodes can allow the catalyst growth in 3D manner, which may increase the effective surface area [21,22]. Importantly, the support should be stable with better internal electrical conductivity for efficient electron movement during the electrochemical performance [23]. As, the electrical conductivity of nickel is 1.43×10^7 S m^{-1}, which is ~6 times higher than titanium (2.38×10^6 S m^{-1}) at 20 °C. (iii) The electrocatalyst directly grown on the electrode surface facilitates an intimate contact, which minimizes the contact resistance of the electrode. In *vice-versa*, it can provide the multiple pathways for proficient charge (e$^-$) transport; more electrons can participate in the electrochemical reactions [24,25]. The utilization of element from support can reduce the catalyst precursor requirement [26]. (iv) The large size anions (O^{2-} < S^{2-} < Se^{2-}) may endowed suitable band gap, thus enhances the electrochemical performance [27].

Lately, the transition metal chalcogenides received much attention as alternative electrocatalysts for water splitting [28–30]. For example, Zhu et al. reported the NiS on nickel foam (NF) catalyst, requires an OER overpotential of 335 mV to afford 50 mA cm^{-2} current density [31]. Wu et al. have achieved the current density of 100 mA cm^{-2} from graphite supported Ni$_{0.85}$Se at 364 mV overpotential [32]. Recently, MoS$_2$ microsphere on NF has explored as OER catalyst by Yan et al., it requires 290 mV overpotential to generate 20 mA cm^{-2} current density [33]. Swesi et al., studied the OER of electrodeposited Ni$_3$Se$_2$ on Au-coated Si substrate, it is needed 290 mV for 10 mA cm^{-2} current density [34]. NiSe on NF has been reported by Tang et al., and it should need an overpotential of 270 mV to reach 20 mA cm^{-2} current density [35]. Liu et al., proposed the electrodeposited Co-S on a Ti mesh as OER catalyst with overpotential of 430 mV for current density of 100 mA cm^{-2} [36]. Fang et al., deposited the Ni$_{2.3}$%-CoS$_2$ on carbon cloth, which needs 370 mV overpotential to reach the current density of 100 mA cm^{-2} [37]. In accordance with these reported results, recently sulfides and selenides based electrocatalysts appear to be promising candidates for OER with a reasonable current density. Even though, the overpotential reported is still larger for the implementation in real scale applications. Moreover, a key point for the large scale application is the electrode durability; unfortunately the durability reported on various electrocatalysts limits their large scale applications. Accordingly, to address the above problems, here we show energy efficient non-precious electrodes with lower anodic overpotential and ultra-durability of 500 h in water electrolyzer. We intuitively used Ni foam as a support as well as Ni source to form a Ni$_3$Se$_2$/NF electrode via an *in-situ* single-step hydrothermal route.

Here, we describe the *in-situ* conversion of Ni foam into Ni$_3$Se$_2$/NF in selenium ions environment *via* pressurized single-step hydrothermal method, and introduce as an alternative energy efficient and ultra-durable anode for water oxidation in strong alkaline electrolyte conditions. Structural and optical analyses confirm the successful formation of cauliflower structured rombhodetral-Ni$_3$Se$_2$/NF electrocatalyst. In 1 M KOH, the Ni$_3$Se$_2$/NF electrocatalyst requires an overpotential of 315 mV to reach the oxygen evolution current density of 100 mA cm^{-2}. Moreover, the OER stability of electrode was tested up to 285 h with 100 mA cm^{-2}, it shows an ultra-durability even at a high current density with a minimum voltage loss of 5.5%. Post-analysis confirms the electrocatalyst and electrode stability after long-term durability test. A step closure to the water splitting, we made a two-electrode alkaline water electrolyzer with NiCo$_2$S$_4$/NF cathode, and it requires a voltage of 1.58 V (vs RHE) to reach the current density of 10 mA cm^{-2} with 5% voltage loss after 500 h continuous operation. It is one of the ultra-durability studies ever reported using a two-electrode alkaline water electrolyzer. In addition, it has cou-

pled with a solar panel for cost free voltage, and demonstrated as a solar-to-hydrogen model for cost-effective hydrogen generation.

2. Experimental section

2.1. Materials

Selenium (Se) powder and ethylenediamine (99%, C$_2$H$_8$N$_2$) were procured from the Alfa Aesar, Korea. All the compounds were used without any further purification. The deionized water was used as a solvent. Ethanol and hydrochloric acid (3 M HCl) were purchased from SAMCHUN, Korea. Nickel foam (>99.99%, 80 μm) was acquired from MTI Korea, explored as a substrate and nickel source.

2.2. Formation of Ni$_3$Se$_2$ on Ni foam

The Ni foam (1 cm × 1 cm) was washed by 3 M HCl, ethanol, and deionized water, respectively to expose the nickel metal by dissolving the surface oxidized nickel. Selenium powder (0.022 g) was dispersed in the mixture of ethylenediamine (25 mL) and deionized water (15 mL) by 30 min sonication. Then, the selenium solution was transferred into the Teflon container, and the cleaned Ni foam (0.0441 g) was immersed into the solution. Then, the Teflon container was closed and kept at 160 °C for 25 h in a Parr autoclave (Model: 4838). After 25 h, the Ni$_3$Se$_2$/NF sample was taken out from the autoclave and rinsed with copious amount of deionized water to remove all unreacted selenium. To remove the moisture, the Ni$_3$Se$_2$/NF was dried under vacuum at 60 °C for overnight. For comparison, NiSe electrocatalyst was also prepared on a Ni foam (NiSe/NF) using 0.05 g of selenium powder under the identical conditions.

2.3. Characterization of Ni$_3$Se$_2$ on Ni foam

The powder X-ray diffraction (Rigaku, MiniFlex 600) was used to find the possible phase formation of various samples. The morphology of the electrocatalyst was examined by FESEM (Hitachi-S4800, 3 kV). The oxidation states of the catalytic elements were investigated through XPS analysis (Thermo-Scientific ESCALAB 250×i) under the vacuum of 10^{-9} mbar, with an exciting source of Mg.

2.4. Electrochemical measurements

The electrochemical tests were executed using Bio-Logic electrochemical workstation. The typical three electrode cell consists of working electrode (the various catalysts on Ni foam), counter electrode (a platinum wire) and reference electrode (a saturated calomel electrode). All experiments were carried out in aqueous electrolyte of 1 M KOH with low scan rate (10 mV s^{-1}) to reduce the capacitive current. In this work, all linear sweep voltammograms (LSV) were iR corrected based on the electrolyte ohmic resistance (R$_s$), except for the durability (three and two electrodes) tests. All the current densities were reported in accordance with electrode geometrical area. The R$_s$ and R$_{ct}$ (charge transfer) resistances with applied bias potential as well as OCV (open circuit voltage) were obtained from electrochemical impedance spectroscopy (EIS) between 100 MHz and 10 mHz frequency range. A simple Randles circuit was fitted with EIS spectra to extract the precise resistance values. Electrochemical active surface area (ECSA) of the Ni foam supported catalysts was attained from double layer capacitance from 100 to 500 mV s^{-1} scan rates using cyclic voltammetry. The two-electrode water splitting set up was constructed with anode (Ni$_3$Se$_2$/NF) and cathode (NiCo$_2$S$_4$/NF), and compared precious and other non-precious electrode systems in 1 M KOH. In addition, the two-electrode water splitting cell was connected with solar panel
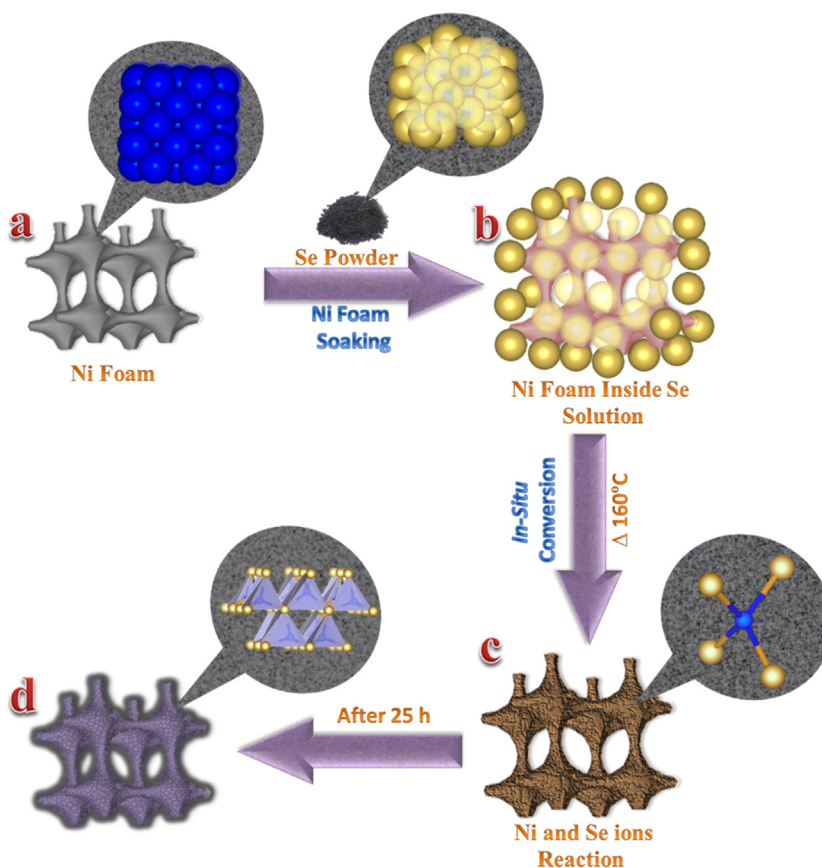
Fig. 1. Ni$_3$Se$_2$/NF formation scheme: (a) bare Ni foam, (b) Ni foam with Se ions, (c) Ni-Se ions interaction, (d) development of Ni$_3$Se$_2$/NF, and its crystal structure (Zoom in).

(MiniSolar co., Ltd.) and demonstrated as a solar-to-hydrogen generation model.

3. Results and discussion

3.1. In-situ *formation of Ni$_3$Se$_2$ on 3D-Ni foam*

Fig. 1 illustrates the schematic representation of the *in-situ* formation of Ni$_3$Se$_2$/NF electrocatalyst by hydrothermal method. The surface cleaned porous 3D Ni foam was used as a support as well as Ni source, and crystal structure displays the closely packed nickel atoms, the Ni—Ni bonds are very short in metallic Ni, as shown in Fig. 1a [38]. To enhance the reaction, the selenium powder was dispersed in the mixture of DI water and ethylenediamine (3:5), and transferred into a Teflon-lined Parr autoclave. Nickel foam was immersed into the solution and surrounded by Se elements (Fig. 1b). At 160 °C, the surface Ni ions of NF react with selenium ions and forming a Ni-Se bonding (Fig. 1c), particularly each Ni atom make a bond with four Se atoms in their crystal structure (Fig. 1c). During 25 h continuous reaction, all the Se ions might have reacted with Ni ions and NF surface has completely converted into Ni$_3$Se$_2$. Fig. 1d shows the surface Ni has reacted with Se and completely converted into Ni$_3$Se$_2$, which is strongly attached with unreacted Ni atoms (NF). The Ni$_3$Se$_2$ crystal structure reveals the tetrahedral arrangement of Ni and Se atoms.

3.2. Characterizations of electrocatalysts

3.2.1. XRD analysis

The planes indexed at their corresponding 2θ values in Fig. 2a reveals the formation of Ni$_3$Se$_2$ phase with rhombohedral crystal structure (JCPDS: 01-085-0754). Three strong characteristic peaks at 2θ values of 44.3, 51.6 and 76.2° are related to the nickel foam substrate (JCPDS: 98-004-3397). The XRD phase analysis confirmed the reaction between selenium and nickel ions towards the formation of pure Ni$_3$Se$_2$ electrocatalyst on Ni foam without any impurities. Fig. 2b demonstrates the nickel atom location and the potential ionic bond between nickel (blue) and selenium (gold) atoms. In the crystal structure, each nickel atom is bonded with four selenium atoms in tetrahedral environment [34]. Fig. S1 shows the diffraction pattern and their corresponding crystal planes of
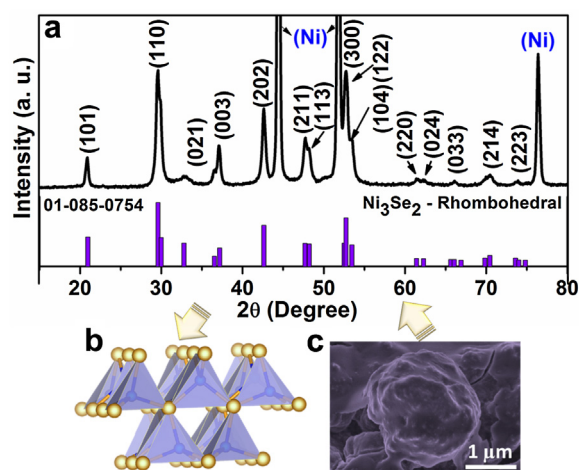

Fig. 2. (a) XRD pattern, (b) crystal structure (Ni-blue, Se-gold), (c) morphology (SEM) of Ni$_3$Se$_2$/NF electrode. (For interpretation of the references to colour in this figure legend, the reader is referred to the web version of this article.)
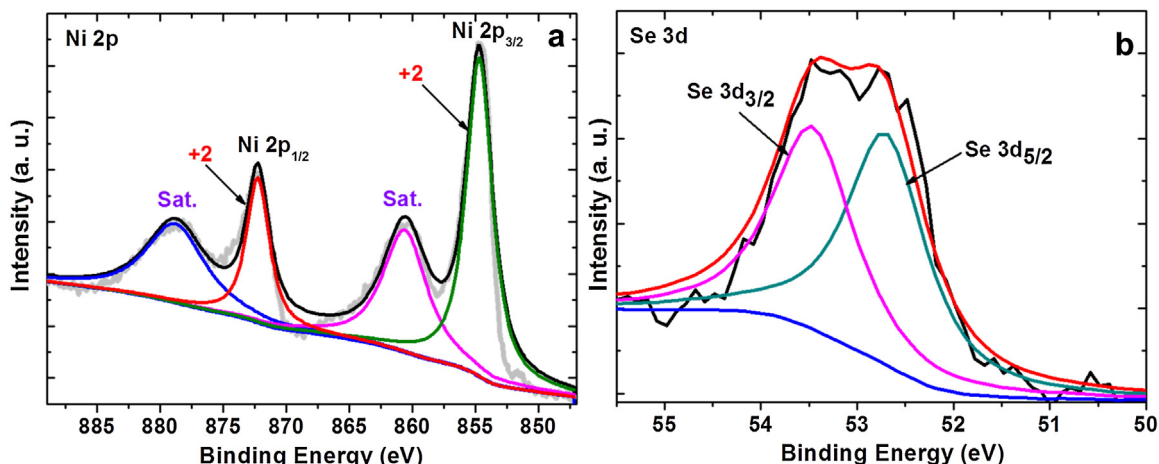
Fig. 3. XPS spectra of (a) Ni 2p, (b) Se 3d of Ni_3Se_2/NF electrode.

rhombohedral-NiSe phase, including 30% of $NiSe_2$ impurity phase formation.

3.2.2. Surface morphology analysis

SEM image in Fig. 2c shows, the successful conversion of Ni foam surface into Ni_3Se_2 electrocatalyst. Fig. S2 shows the surface morphology of bare Ni foam and *in-situ* formed Ni_3Se_2/NF electrocatalyst. Fig. S2a displays the smooth surface of porous 3D-Ni foam electrode (before conversion). Fig. S2b and c are the low magnification images of electrode surface, which reveal the uniform formation of porous Ni_3Se_2 electrocatalyst with multiple pores. The high magnification image shows the cauliflower shaped morphology of the electrocatalyst with bumpy surface (Fig. S2d). The size of the each shape is ~1.5 μm, and the size of the pore is ~300 nm. It is clear that, this porous electrode with rough surface can increase the electrochemical performance of the catalyst due to the exposure of more active sites and electrolyte accessibility. Besides, it can make good path to escape the formed gas bubbles from the electrode surface without any physical damage of the electrocatalyst material on the surface of the electrode. Another important phenomenon is that, this kind of converted Ni_3Se_2/NF has strong connection with substrate than the deposition of both Ni and Se ions on the electrode surface. More clearly, Se ions can interact with substrate Ni ions and forming the Ni_3Se_2/NF electrocatalyst. Compared with other morphologies of the catalysts such as nanorods [39], nanowires [40], and nanotubes [41], this kind of morphology is more stable from the chemical and physical disturbances.

3.2.3. XPS analysis

The various electronic states of Ni and Se elements in the near surface region of as-synthesized Ni_3Se_2/NF electrocatalyst are further investigated using X-ray photoelectron spectroscopy. The Ni 2p spectrum of the Ni_3Se_2 electrocatalyst is de-convoluted into $2p_{3/2}$ and $2p_{1/2}$ doublets due to spin-orbit coupling with two shakeup satellite peaks (Fig. 3a). In peak fitting analysis, the binding energy at 854.7 eV for Ni $2p_{3/2}$ and 872.1 eV for Ni $2p_{1/3}$ are spin orbit characteristics of Ni^{2+} ion [42]. The Ni 2p spectrum also exclude the possible existence of Ni^{3+}. It clearly reveals that, the most of Ni exists in the form of Ni^{2+} state. The appearance of intense satellite peaks at 861.3 and 879.2 eV in the Ni 2p spectrum is another evidence for predominant existence of Ni^{2+} in Ni_3Se_2 electrocatalyst (Fig. 3a) [43]. Fig. 3b shows the detailed analysis of Se 3d high resolution XPS spectra. In particular, the Se 3d spectrum of Ni_3Se_2 can be well fitted with $3d_{5/2}$ and $3d_{3/2}$ doublet peaks. In specific, the doublet energy separation is ~0.8 V, which perfectly matches with the standard observation [44]. So, it confirms the −2

valance state of Se (Se^{2-}) and which makes only one kind of possible metal-selenide bond (Ni—Se) [35]. From these observations, we believe that the successful formation of Ni-Se compound in the form of Ni_3Se_2, which is also confirmed from XRD analysis (Fig. 2a).

3.3. Electrochemical activity

3.3.1. Oxygen evolution reaction (OER)

3.3.1.1. Linear sweep voltammograms (LSVs). First, the OER activity of the prepared electrocatalyst is evaluated using a three electrode set up, with a scan rate of $10\,mV\,S^{-1}$ in 1 M KOH. Fig. 4a shows the OER LSVs of Ni_3Se_2/NF NiSe/NF, NF and RuO_2/GC electrodes in O_2-saturated 1 M KOH. The OER current density and potential is normalized to the geometrical area of the working electrode and compensated with solution resistance (iR), respectively. In Fig. 4a, the intense oxidation peak has noticed at ~1.38 V due to the Ni(II)-Ni(III) conversion during the electrochemical performance. It is evidenced that, the surface Ni atoms has partially oxidized into NiOOH on the surface of Ni_3Se_2/NF electrode. An interestingly, the oxidation peak is higher than other electrocatalysts, implying the formation of more active sites (NiOOH) on Ni_3Se_2/NF surface [45]. Due to the intense Ni oxidation [Ni(II) to Ni(III)] peak at ~1.38 V the oxygen evolution overpotential measurement at $10\,mA\,cm^{-2}$ is difficult or not accurate. Thus, here we have reported the overpotential at higher current density ($100\,mA\,cm^{-2}$). Institutively formed rhombohedral Ni_3Se_2/NF electrode affords $100\,mA\,cm^{-2}$ OER current density at 315 mV overpotential (Table 1). In the case of, NiSe/NF and RuO_2/GC electrodes require the overpotential of 411 mV and 420 mV respectively to attain $100\,mA\,cm^{-2}$, and bare NF shows very less current density (~$50\,mA\,cm^{-2}$) even at 1.7 V. The specific activities of all the electrocatalysts are calculated from OER curves at 1.60 V (Fig. S3) and compared in Table 1. In addition, the Ni_3Se_2/NF electrocatalyst shows higher value of $241.1\,mA\,cm_{(geo)}^{-2}$, which is 8 and 5 times higher than RuO_2/GC

Table 1
OER overpotential, Tafel slope and specific activity comparison of various synthesized electrocatalysts.

Catalyst	OER Overpotential (mV vs RHE) @ 100 mA cm^{-2}	Tafel Slope (mV dec^{-1})	Specific Activity (mA cm$_{(geo)}^{-2}$) @ 1.60 V vs RHE
Ni_3Se_2/NF	315	40.2	241.1
NiSe/NF	411	59.4	49.8
RuO_2	420	52.1	29.7
NF	–	94.1	6.2

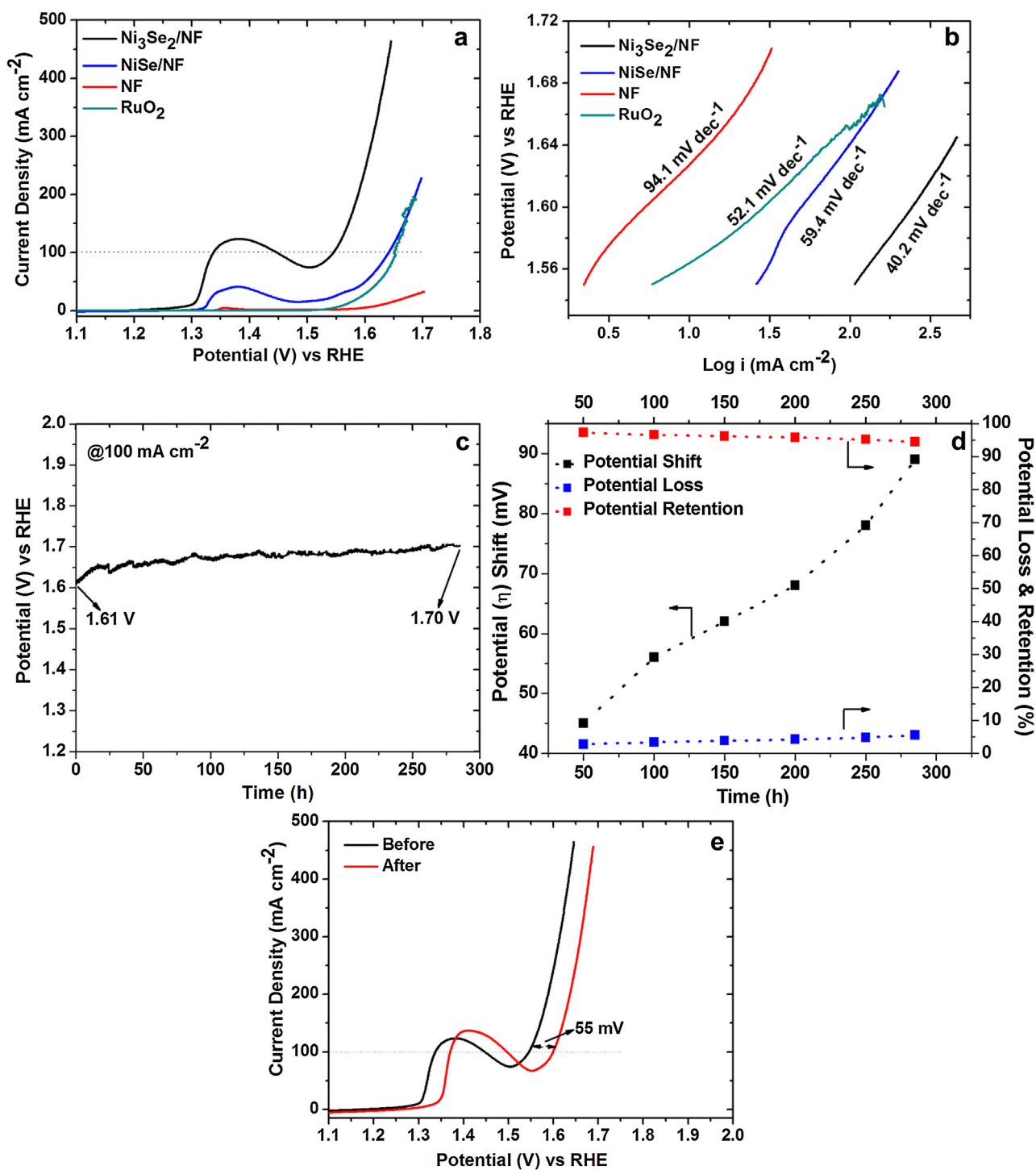**Fig. 4.** Electrochemical performance in 1 M KOH: (a) OER LSV curves (iR-compensated) of Ni_3Se_2/NF, $NiSe/NF$, NF and RuO_2/GC (scan rate: 10 mV s^{-1}), (b) corresponding Tafel plots, (c) chronopotentiometry durability test (without iR-compensated) at a constant current density of 100 mA cm^{-2}, (d) potential shift and corresponding potential loss and retention during 285 h durability test, (e) linear sweep voltammograms before and after 285 h chronopotentiometry durability test (scan rate: 10 mV s^{-1}).

and NiSe/NF electrocatalyst, respectively. It can be clearly seen from Table 1, that the catalytic activity of Ni_3Se_2/NF electrocatalyst is highly enhanced, which can attributed to increase the surface area and the formation active species. Also, the Ni_3Se_2/NF electrode is active for hydrogen evolution reaction, exhibits the onset overpotential of 150 mV in same alkaline environment (1 M KOH) as shown in Fig. S4. So, this observation reveals that, Ni_3Se_2/NF electrocatalyst has favorable activity for overall water splitting.

This comparison clearly reveals that the Ni_3Se_2/NF electrocatalyst exhibits very low overpotential than precious electrocatalyst RuO_2/GC, and the difference in the overpotential is ∼105 mV, which is vast difference among at 100 mA cm^{-2}. Furthermore, as compared with recently reported electrocatalysts, such as NiS/NF [29], Ni-Co-S/CF (Cu foam) [46], CoSe/GC (glassy carbon) [47] and other electrocatalysts, particularly $Ni_{2.3\%}CoS_2/CC$ [35], Co_9S_8/N-C(Nitrogen-Carbon) matrix [48] are required huge overpotential to

obtain 100 mA cm^{-2} (Table S1). Accordingly, Ni$_3$Se$_2$/NF electrode needs very low overpotential to achieve high anodic current density.

3.3.1.2. Tafel slope. Obviously, the obtained OER Tafel slope value also explains the possible and favorable OER kinetics for the enhanced performance of Ni$_3$Se$_2$/NF electrocatalyst than other electrocatalysts. Fig. 4b, Ni$_3$Se$_2$/NF electrode displays the Tafel slope value of 40.2 mVdec^{-1}. However, Tafel slope values for NiSe/NF and RuO$_2$/GC are found to be 59.4 and 52.1 mVdec^{-1}, respectively. Comparatively, it is lower than bare NF, which exhibits very high Tafel slope of 94.1 mVdec^{-1}. Accordingly, Ni$_3$Se$_2$/NF electrode exhibits very low Tafel slope compared with other electrocatalysts, and the results clearly evident that the Ni$_3$Se$_2$/NF electrode has a facile OER kinetics. In addition, according to Tafel slope, we can able to predict the rate-determining step for OER. Tafel slope of 120 mVdec^{-1} offers the step just before the rate-determining stage, at this stage the surface species formation may occur rather than rate-determination process [49]. If, the Tafel slope value is less than 120 mVdec^{-1}, it may involve in the OER rate-determination kinetics. In general, OER is a complicated 2 or 4 electron transfer process.

3.3.1.3. Ni$_3$Se$_2$ electrode durability test. Moreover, the electrochemical stability of electrocatalyst is another important issue in the real scale hydrogen generation, due to the continuous electrochemical reactions, the gas evolutions occur in the electrolyte environments. Accordingly, to understand the changes in potential, phase and surface morphology, we have evaluated the long term durability of Ni$_3$Se$_2$/NF electrode *via* chronopotentiometry at 100 mA cm^{-2}. Fig. 4c and d show 285 h continuous durability plot and their potential shift (without iR-correction) with potential loss and retention (%) for the each 50 h period, respectively. Initially, Ni$_3$Se$_2$/NF electrode affords the OER current density of 100 mA cm^{-2} at ∼1.61 V. To be specific, up to ∼10 h the rapid increment has noticed in the potential from ∼1.61 to ∼1.66 V (Fig. 4c), which may be due the partial wettability of the electrode surface and the new environment of electrode. However, after certain duration, it shows almost stable potential with very small loss even after 285 h continuous durability test at 100 mA cm^{-2}. For interpretation of small changes and comparison, the potential shift, potential loss and retention *vs* time is plotted in Fig. 4d. The potential plot (black line) demonstrates that the potential shift from ∼45 (at 50 h) to ∼90 mV (at 285 h). On this occurrence, since 50 to 100 h, the potential increased rapidly from ∼45 to ∼57 mV in accordance with time. But, after 100 h, the potential change is negligible and gradually increased when compared with previous stage. Over 250 h, the potential is increased rapidly from ∼77 to ∼90 mV within 35 h. In addition, the potential loss (blue line) and retention (red line) also calculated and displayed in Fig. 4d. At 50 h, the potential loss is very small (1%), even after 100 h the loss is increased gradually up to 285 h, at the end the maximum potential loss is 5.5% or *vice versa* 94.5% retention. Hence, only 5.5% potential loss after 285 h long term durability at 100 mA cm^{-2} is negligible for real, large scale application, and this loss may due to the vigorous oxygen evolution on the electrode surface. Further confirmation for the stability of Ni$_3$Se$_2$/NF electrocatalyst after 285 h durability test, we measured the overpotential shift (with iR-correction) for fresh and after 285 h test by overlaying LSV traces (Fig. 4e). As compared with fresh electrocatalyst overpotential (315 mV), it needs an extra overpotential of 55 mV (370 mV) to afford the 100 mA cm^{-2}. Accordingly, low overpotential shift in LSV measurement also confirms the stability of Ni$_3$Se$_2$/NF electrocatalyst electrode.

3.3.1.4. Ni$_3$Se$_2$ electrode post mortem analysis. Also, we examine the reason for small increment in the overpotential by post anal-

yses using XRD, SEM, XPS, EIS and ECSA for Ni$_3$Se$_2$/NF electrode after durability test. The post-XRD observation reveals that the rombhohedral-Ni$_3$Se$_2$ phase has still maintained even after 285 h continuous durability test (Fig. S5b). The intensity of the nickel phase from nickel foam has increased slightly, due to nickel foam exposure by small variation in electrode morphology. Fig. S6 clearly demonstrates the noticeable morphology variation of electrocatalyst from cauliflower shape to small particle clusters, without any peeling off from the electrode surface (post-SEM). Of course, it is possible during vigorous and nonstop evolution of oxygen gas bubbles on electrode surface [50]. In Fig. S7, the post-Ni 2p XPS spectra exposes the same binding energies at 854.9 and 872.6 eV for spin orbit characteristics of Ni^{2+} as well as peak broadening, with existence of intense satellite peak similar to the fresh sample. After the peak fitting analysis, new peaks appear at two different binding energies at 856.3 and 873.9 eV are due to the NiOOH formation on electrode surface (Fig. S7a) [51]. Similarly, Se 3d post-XPS spectra (Fig. S7b) depict the major conversion of selenium into selenium oxide; it is possible only with surface selenium, confirmed in post-XRD study (Fig. S5b). The post-EIS result shows the R$_{ct}$ value of 2.6 Ω (Fig. S8), slightly higher than fresh sample R$_{ct}$ value (1.75 Ω). The calculated electrochemical active surface area from post-ECSA measurement (3.3 mF cm^{-2}) is evident that, there is no major change in the electrode surface area (Fig. S9).

3.3.2. Electrochemical impedance analysis

An electrochemical measurement in the electrolyte medium has a few unavoidable factors which can be disturb the electrocatalytic activity of the catalyst. To be specific, the ionic and charge transport resistances are the most key factors, which can increase the reaction barrier during the water electrolysis. To know these elements quantitatively during the oxygen evolution reaction, we recorded Nyquist (1 M KOH) plots at open circuit voltage (OCV) and the biased potential of 1.597 V versus RHE as shown in Fig. 5. Also, the Randles equivalent circuit (Fig. 5a (inset)) was used to fit the EIS spectra and to evaluate the precise values of the electrolyte resistance (R$_s$) in higher frequency region, charge transfer resistance (R$_{ct}$) in lower frequency region including double layer capacitance (C$_{dl}$) of the electrode. From the Z-fitted curve (Fig. 5a), we obtained the R$_s$ and R$_{ct}$ values of ∼2 Ω and ∼1.75 Ω, respectively, comparatively it is lower than other reported electrocatalyst electrode [52,53]. Accordingly, the *in-situ* formation of Ni$_3$Se$_2$/NF clearly reveals that, it is more favorable for the electron transfer, and which can remarkably assist to overcome the reaction barrier during the OER in 1 M KOH. Moreover, this electrolyte resistance is used for iR-correction of all OER linear sweep voltammograms.

3.3.3. Cyclic voltammograms (electrochemical active surface area analysis)

Electrochemical active surface area (ECSA) is another important additional evidence of superior OER activity of Ni$_3$Se$_2$/NF electrode, which is calculated on the basis of the measured electrical double-layer capacitance (EDLC) of Ni$_3$Se$_2$/NF electrode in 1 M KOH [54]. Fig. 5b shows the cyclic voltammograms (CV) with various scan rates (100–500 mV s^{-1}) between the potential of 0.63 V–0.73 V (vs RHE). At each scan rate, CV curve shows the perfect rectangular behavior, it confirms the existence of double layer capacitance, it may be because of high electrochemical active surface area of the electrode. As noticed that, from lower scan rate to higher scan rate, the anodic (i$_a$) and cathodic (i$_c$) current densities (CV areas) have linearly increased up to 2 mA cm^{-2}. To be specific, for more interpretation and calculation we measured the values of i$_a$ and i$_c$ at the potential of 0.68 V versus RHE from each rectangular CV spectra. The current density versus scan rate is plotted, and also linearly fitted using a linear fit, which is shown in Fig. 5c. It exhibits the capacitance value of 3.6 mF cm^{-2}, and also
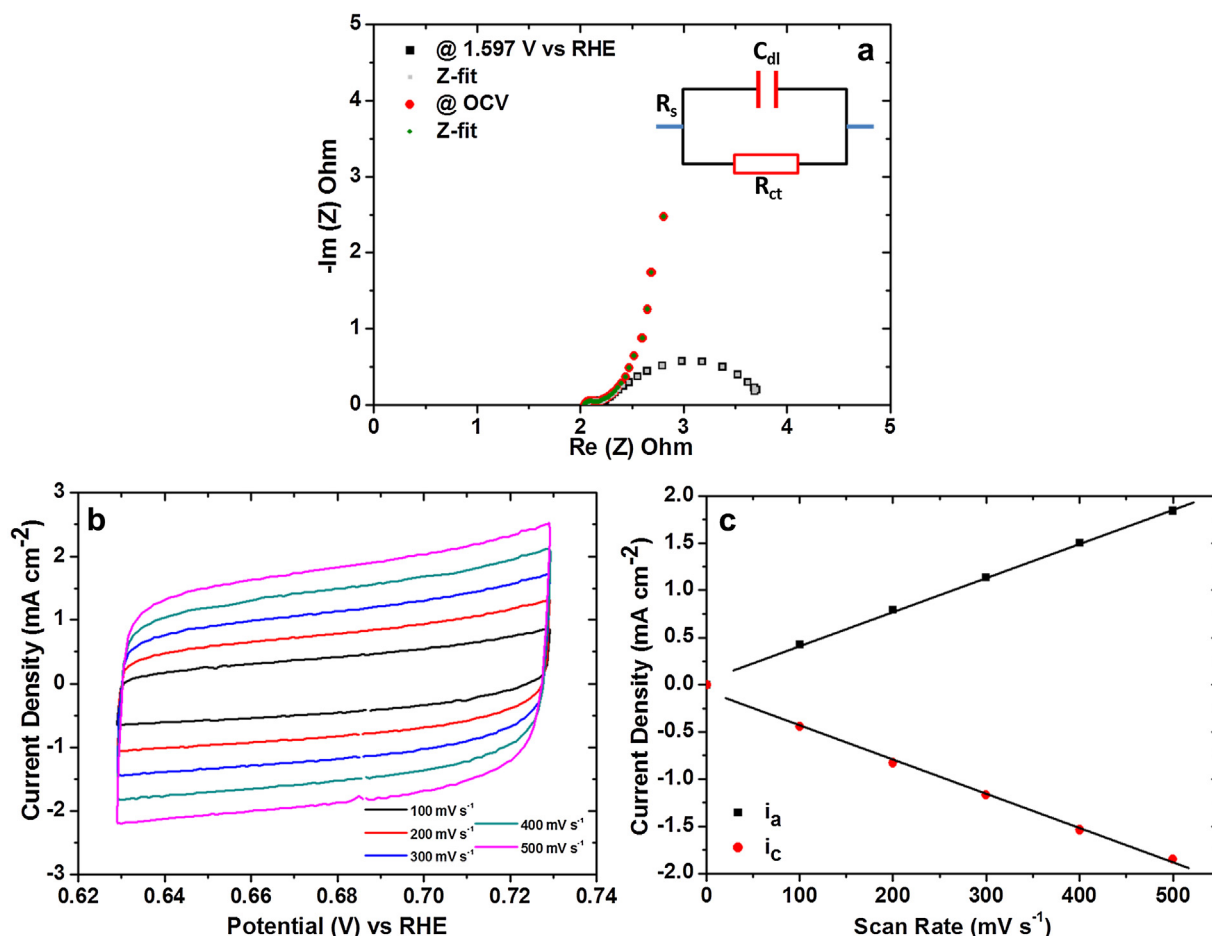
Fig. 5. (a) EIS spectra for Ni_3Se_2/NF electrode at OCV and 1.597 V (vs RHE) in 1 M KOH, (b) cyclic voltammograms for Ni_3Se_2/NF electrode at the scan rate of 100, 200, 300, 400 and 500 mV s^{-1} in 1 M KOH, (c) linear fitted curve of corresponding capacitive currents at 0.68 V (vs RHE).

the obtained electrochemical surface area and roughness factor is 16.2 cm^2 and 90, respectively for the Ni_3Se_2/NF electrode, which has good agreement with SEM surface morphology (Fig. S2d). So, the high roughness factor helps to increase the electrolyte interaction with electrocatalyst. Hence, the *in-situ* grown electrocatalyst on a 3D Ni foam is to overcome the few unavoidable factors and helps to improve the OER kinetics of Ni_3Se_2/NF electrode for the superior activity with low overpotential.

3.3.4. Two-electrode alkaline water electrolyzer study

Close to the real scale application for the large scale production of pure hydrogen, we have constructed the two-electrode set up, and tested the performance in 1 M KOH environment. Fig. 6a shows the optical image of two electrodes alkaline water electrolyzer arrangement with electrolyte during the overall water splitting operation. The both electrode active area exposed in the electrolyte is 1.8 cm^2. The cathode material $NiCo_2S_4$/NF has selected based on its excellent HER activity [55]. In Fig. 6b, LSVs show the cell voltage (with iR-compensated) of non-precious and precious electrocatalyst based alkaline water electrolyzer. The Ni_3Se_2/NF//$NiCo_2S_4$/NF cell requires 1.58 V to afford the 10 mA cm^{-2} current density, but, the commercial precious catalyst system RuO_2/NF//Pt/C/NF needs less voltage of 1.53 V to reach 10 mA cm^{-2}. It confirms that, the non-precious electrodes require 50 mV extra voltage than precious electrodes to obtain 10 mA cm^{-2}. However, the obtained voltage value is very close to the voltage of precious electrocatalyst, also it is strikingly lower than recently reported non-precious electrodes, particularly bifunctional electrocatalysts (see Table S2). The long

term durability test was carried out for the same two electrodes set up as shown in Fig. 6c. Initially, it requires 1.76 V (without iR-compensated) to delivered 10 mA cm^{-2} and then within 10 h it increased gradually up to 1. 8 V. After 10 h, the voltage has maintained without major increment up to 365 h, and then it was increased gradually up to 1.82 V at 500 h continuous durability test. At the end, after 500 h durability test, it needs only 1.82 V to afford 10 mA cm^{-2}. Similarly, corresponding voltage value for different current densities also measured for Ni_3Se_2/NF//$NiCo_2S_4$/NF electrode, which is shown in Fig. S10. It requires the cell voltages of 1.72, 1.83, 1.86, 1.93 and 1.98 V to afford the different current densities from 20 to 50 mA cm^{-2}, respectively.

3.3.5. Demonstration of solar-to-hydrogen generation

The water electrolysis using the voltage from solar energy is one of the energy efficient ways to increase the production of hydrogen [56]. Accordingly, the solar energy utilized alkaline water electrolysis in 1 M KOH (through a solar panel) has schematically demonstrated in Fig. 7, and optical image is shown in Fig. S11. Due to the higher open circuit voltage and current density of GaAs thin film solar cell, it can produce a maximum voltage of 3.65 V depends on the distance from the light source (Fig. S12). Because of this reason, in our study, we have used this solar cell as a voltage producer for solar-to-hydrogen generation. The LED desk night-light (18W) was used as a light source, implying that we explored the usage of street light energy for continuous hydrogen production even at night time. In scheme and optical image (Fig. 7 and S11), the Ni_3Se_2/NF anode and $NiCo_2S_4$/NF cathode in two-electrode

Fig. 6. Two electrodes setup (Ni_3Se_2/NF//$NiCo_2S_4$/NF) in 1 M KOH: (a) optical image of Ni_3Se_2/NF (anode) and $NiCo_2S_4$/NF (cathode) in the electrolyte, generating O_2 and H_2 gas evolution, respectively, (b) LSVs (scan rate: $10\,mV\,s^{-1}$), (c) chronopotentiometry durability test (without iR-compensated) at a constant current density of $10\,mA\,cm^{-2}$.

alkaline water electrolyzer set-up was connected to the positive and negative terminals of solar panel, respectively, through a less-resistive crocodile-clip. The voltage applied to the alkaline water electrolyzer from a solar panel is monitored through a digital mul-

timeter, which is connected to the same crocodile-clip. Light source and solar panel distance was maintained to produce the stable voltage of 1.60 V, which was supplied to the alkaline water electrolyzer. At 1.60 V, we noticed the continuous oxygen and hydrogen evo-
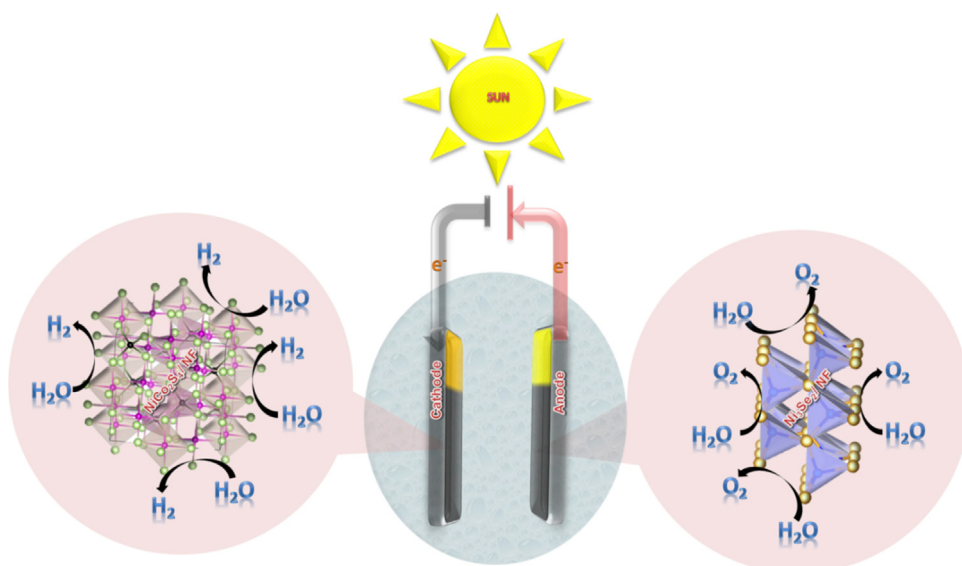

Fig. 7. Solar panel assisted solar-to-hydrogen generation of Ni_3Se_2/NF//$NiCo_2S_4$/NF water electrolyzer in 1 M KOH aqueous electrolyte.

lution in Ni_3Se_2/NF electrode (anode) and $NiCo_2S_4$/NF electrode (cathode), respectively (Movie S1). Hence, this non-precious electrodes utilized solar energy assisted alkaline water electrolysis is a cost-effective method (free of electricity) for the production of hydrogen in real, large scale hydrogen generation.

4. Conclusion

Inexpensive, efficient and ultra-durable *in-situ* formed Ni_3Se_2/NF electrode was proposed as a potential anode for water splitting. *In-situ* developed electrode displays more favorable charge transfer resistance and electrochemical active surface area in strong alkaline electrolyte. Obtained favorable factors enhances the oxygen evolution and durability, it affords $100\,mA\,cm^{-2}$ current density at $315\,mV$ overpotential, and $285\,h$ continuous durability without any major variation in the applied potential. In full water splitting using non-precious $NiCo_2S_4$/NF cathode, it requires only $1.58\,V$ to achieve $10\,mA\,cm^{-2}$ current density, then $500\,h$ ultra-durability in water electrolyzer. Solar-to-hydrogen approach using earth abundant, cost effective non-precious electrodes are the key concern to entirely replacement of precious electrocatalyst in real, large scale solar-to-hydrogen generation.

Acknowledgement

Appendix A. Supplementary data

Supplementary data associated with this article can be found, in the online version, at http://dx.doi.org/10.1016/j.apcatb.2016.10.050.

References

[1] M.P. Browne, H. Nolan, G.S. Duesberg, P.E. Colavita, M.E.G. Lyons, ACS Catal. 6 (2016) 2408–2415.
[2] H.S. Oh, H.N. Nong, T. Reier, M. Gliech, P. Strasser, Chem. Sci. 6 (2015) 3321–3328.
[3] K. Zeng, D. Zhang, Prog. Energ. Combust. 36 (2010) 307–326.
[4] B.C.M. Martindale, E. Reisner, Adv. Energy Mater. 6 (2016) 1502095.
[5] J. Luo, J.H. Im, M.T. Mayer, M. Schreier, M.K. Nazeeruddin, N.G. Park, S.D. Tilley, H.J. Fan, M. Gratzel, Science 345 (2014) 1593–1596.
[6] F. Song, K. Schenk, X. Hu, Energy Environ. Sci. 9 (2016) 473–477.
[7] H. Dau, C. Limberg, T. Reier, M. Risch, S. Roggan, P. Strasser, ChemCatChem 2 (2010) 724–761.
[8] N.S. Lewis, D.G. Nocera, Proc. Natl. Acad. Sci. U. S. A. 103 (2006) 15729–15735.
[9] S. Hyun, V. Ahilan, H. Kim, S. Shanmugam, Electrochem. Commun. 63 (2016) 44–47.
[10] Y. Xiao, L. Feng, C. Hu, V. Fateev, C. Liua, W. Xing, RSC Adv. 5 (2015) 61900–61905.
[11] T. Maiyalagan, K.A. Jarvis, S. Therese, P.J. Ferreira, A. Manthiram, Nat. Commun. 5 (2014) 3949.
[12] M.A.D. Crespo, M.P. Torres, A.M.T. Huerta, C.R. Rodriguez, E.M.A. Estrada, ECS Trans. 3 (2006) 135–148.
[13] W.N. Su, D.W. Ayele, V. Ochie, C.J. Pan, B.J. Hwang, Appl. Catal. B: Environ. 150–151 (2014) 363–369.
[14] B. You, N. Jiang, M. Sheng, S. Gul, J. Yano, Y. Sun, Chem. Mater. 27 (2015) 7636–7642.
[15] X. Cui, P. Ren, D. Deng, J. Deng, X. Bao, Energy Environ. Sci. 9 (2016) 123–129.
[16] Z. Jiang, Z.J. Jiang, T. Maiyalagan, A. Manthiram, J. Mater. Chem. A 4 (2016) 5877–5889.
[17] S. Ghosh, P. Kar, N. Bhandary, S. Basu, S. Sardar, T. Maiyalagan, D. Majumdar, S.K. Bhattacharya, A. Bhaumik, P. Lemmens, S.K. Pal, Catal. Sci. Technol. 6 (2016) 1417–1429.
[18] J. Qi, W. Zhang, R. Xiang, K. Liu, H.Y. Wang, M. Chen, Y. Han, R. Cao, Adv. Sci. 2 (2015) 1500199.
[19] M. Ledendecker, G. Clavel, M. Antonietti, M. Shalom, Adv. Funct. Mater. 25 (2015) 393–399.
[20] W. Yan, X. Cao, K. Ke, J. Tian, C. Jina, R. Yang, RSC Adv. 6 (2016) 307–313.
[21] S.H. Lee, E.J. Lim, Y.R. Jo, B.J. Kim, W.B. Kim, ACS Appl. Mater. Interfaces 6 (2014) 20634–20642.
[22] P. Li, Z. Jin, J. Yang, Y. Jin, D. Xiao, Chem. Mater. 28 (2016) 153–161.
[23] W.Y. Xia, N. Li, Q.Y. Li, K.H. Ye, C.W. Xu, Sci. Rep. 6 (2016) 23398.
[24] H.F. Wang, C. Tang, X. Zhu, Q. Zhang, J. Mater. Chem. A 4 (2016) 3379–3385.
[25] D. Pan, M. Ombaba, Z.Y. Zhou, Y. Liu, S. Chen, J. Lu, ACS Nano 6 (2012) 10720–10726.
[26] N. Feng, D. Hu, P. Wang, X. Sun, X. Li, D. He, Phys. Chem. Chem. Phys. 15 (2013) 9924–9930.
[27] T. Jing, Y. Dai, X. Ma, W. Wei, B. Huang, J. Phys. Chem. C 119 (2015) 27900–279008.
[28] B. Chen, R. Li, G. Ma, X. Gou, Y. Zhu, Y. Xia, Nanoscale 7 (2015) 20674–20684.
[29] L. Yang, M. Gao, B. Dai, X. Guo, Z. Liu, B. Peng, Electrochim. Acta 191 (2016) 813–820.
[30] P. Ganesan, M. Prabu, J. Sanetuntikul, S. Shanmugam, ACS Catal. 5 (2015) 3625–3637.
[31] W. Zhu, X. Yue, W. Zhang, S. Yu, Y. Zhang, J. Wang, J. Wang, Chem. Commun. 52 (2016) 1486–1489.
[32] X. Wu, D. He, H. Zhang, H. Li, Z. Li, B. Yang, Z. Lin, L. Lei, X. Zhang, Int. J. Hydrogen Energy 41 (2016) 10688–10694.
[33] K. Yan, Y. Lu, Small 12 (2016) 2975–2981.
[34] A.T. Swesi, J. Masud, M. Nath, Energy Environ. Sci. 9 (2016) 1771.
[35] C. Tang, N. Cheng, Z. Pu, W. Xing, X. Sun, Angew. Chem. Int. Ed. 54 (2015) 9351–9355.
[36] T. Liu, Y. Liang, Q. Liu, X. Sun, Y. He, A.M. Asiri, Electrochem. Commun. 60 (2015) 92–96.
[37] W. Fang, D. Liu, Q. Lu, X. Sun, A.M. Asiri, Electrochem. Commun. 63 (2016) 60–64.
[38] G.V. Gibbs, R.T. Downs, C.T. Prewitt, K.M. Rosso, N.L. Ross, D.F. Cox, J. Phys. Chem. B 109 (2005) 21788–21795.
[39] G.Q. Han, Y.R. Liu, W.H. Hu, B. Dong, X. Li, X. Shang, Y.M. Chai, Y.Q. Liu, C.G. Liua, J. Electrochem. Soc. 163 (2016) H67–H73.
[40] L. Liao, S. Wang, J. Xiao, X. Bian, Y. Zhang, M.D. Scanlon, X. Hu, Y. Tang, B. Liu, H.H. Girault, Energy Environ. Sci. 7 (2014) 387–392.
[41] M. Tavakkoli, T. Kallio, O. Reynaud, A.G. Nasibulin, J. Sainio, H. Jiang, E.I. Kauppinen, K. Laasonen, J. Mater. Chem. A 4 (2016) 5216–5222.
[42] L. Qian, W. Chen, R. Huang, D. Xiao, RSC Adv. 5 (2015) 4092–4098.
[43] L. Mi, W. Wei, S. Huang, S. Cui, W. Zhang, H. Hou, W. Chen, J. Mater. Chem. A 3 (2015) 20973–20982.
[44] C. Xia, Q. Jiang, C. Zhao, M.N. Hedhili, H.N. Alshareef, Adv. Mater. 28 (2016) 77–85.
[45] K. Xu, P. Chen, X. Li, Y. Tong, H. Ding, X. Wu, W. Chu, Z. Peng, C. Wu, Y. Xie, J. Am. Chem. Soc. 137 (2015) 4119–4125.
[46] T. Liu, X. Sun, A.M. Asiri, Y. He, Int. J. Hydrogen Energy 42 (2016) 7264–7269.
[47] M. Liao, G. Zeng, T. Luo, Z. Jin, Y. Wang, X. Kou, D. Xiao, Electrochim. Acta 194 (2016) 59–66.
[48] X. Cao, X. Zheng, J. Tian, C. Jin, K. Ke, R. Yang, Electrochim. Acta 191 (2016) 776–783.
[49] T. Shinagawa, A.T.G. Esparza, K. Takanabe, Sci. Rep. 5 (2015) 13801.
[50] X. Lv, Y. Zhu, H. Jiang, X. Yang, Y. Liu, Y. Su, J. Huang, Y. Yao, C. Li, Dalton Trans. 44 (2015) 4148–4154.
[51] J. Jiang, C. Zhang, L. Ai, Electrochim. Acta 208 (2016) 17–24.
[52] S. Talu, S. Solaymani, M. Bramowicz, N. Naseri, S. Kulesza, A. Ghaderi, RSC Adv. 6 (2016) 27228–27234.
[53] I.M. Mosa, S. Biswas, A.M.E. Sawy, V. Botu, C. Guild, W. Song, R. Ramprasad, J.F. Rusling, S.L. Suib, J. Mater. Chem. A 4 (2016) 620–631.
[54] X. Lu, C. Zhao, Nat. Commun. 6 (2015) 6616.
[55] A. Sivanantham, P. Ganesan, S. Shanmugam, Adv. Funct. Mater. 26 (2016) 4661–4672.
[56] J. Luo, D.A. Vermaas, D. Bi, A. Hagfeldt, W.A. Smith, M. Gratzel, Adv. Energy Mater. (2016), http://dx.doi.org/10.1002/aenm.201600100.